Inviscid flow passing a lifting body with a higher order boundary element method

Shi Yan Sun[1] **and G.X. Wu**[2, *]

[1] *School of Naval Architecture & Ocean Engineering, Jiangsu University of Science and Technology, Zhenjiang 212003, China*

[2] *Department of Mechanical Engineering, University College London, Torrington Place, London WC1E 7JE, UK*

Abstract: A higher order boundary element method (HOBEM) is presented for inviscid flow passing a lifting body. In addition to the boundary integral equation used for the velocity potential, similar integral equation is derived and used for the tangential velocity on the body surface. Higher order elements are used to discretize the body surface, which ensures the continuity of slope at the element nodes. The velocity potential is also expanded using higher order shape function, in which the unknown coefficients involve the tangential velocity. The expansion then ensures the continuity of the velocity at element nodes and it also allows the Kutta condition to be imposed directly through the velocity. A particular shape function is also derived and used near the trailing edge to account for the continuity of the velocity and its sharp variations there. The unknown potential and tangential velocity are then found through solving their integral equations simultaneously. Through extensive comparison of the results for a Karman-Trefftz (KT) foil, it is shown that the present HOBEM is much more accurate than the conventional BEM, in particular for the velocity and local results near the trailing edge.

Key words: Higher order boundary element method (HOBEM), Kutta condition, Integral equations for potential and velocity, Hydrofoil

1. Introduction

Boundary element methods (BEM) have been extensively used for many decades for irrotational flows passing a solid body. One of its advantage is that it converts the problem of a differential equation in the fluid domain into a problem of an integral equation using the Green function over its boundary and therefore reduces the dimensions of the problem by one. In particular, if apart from the body surface, other boundaries are at infinity, it is often possible that the problem reduces to one on the body surface only. This greatly improves the computational efficiency.

Irrotational flow is usually described through the velocity potential whose gradient is velocity itself, and the integral equation is established for the potential. For a smooth body without any sharp corners, both the potential and the velocity are finite and continuous. The mathematical problem of the integral equation is usually well posed. The flow in such a case does not generate any force on the body, which is commonly known as D'Alembert's paradox. When there is a corner on the surface,

* Corresponding author.
Email address: g.wu@ucl.ac.uk (G.X. Wu)

the flow direction at the corner changes suddenly. This leads to an infinite acceleration, pressure gradient as well as velocity at the corner. A typical example of this is a two dimensional hydrofoil. The mathematical problem of the integral equation in this case becomes ill posed. The root of this problem is the irrotational flow itself, in which both viscosity and vortex are ignored. One way to account for their effects is to use the well known Kutta condition which assumes that vorticity will be shed from the sharp corner and the strength of the vorticity is uniquely obtained through ensuring that the velocity at the corner is finite. In such a case, flow will normally generate a force on the body, especially the lift force or the force perpendicular to the incoming flow direction. The body is commonly known as the lifting body.

For flow passing a hydrofoil, it will be initially transient as the vortex is shed from the trailing edge [1]. The flow will tend to steady as time tends to infinity. The flow is no longer irrotational. One way to model that is to introduce a straight line S_W starting from the trailing edge to infinity along the flow direction. The potential ϕ is no longer continuous across the line and there is a jump of $\Delta\phi_w$. When the integral equation is developed, it will contain both sides of S_W, apart from the body surface. As the normal velocity S_W must be continuous due to mass conversation, its integration from both sides of S_W will cancel each other. Also the pressure across S_W must be continuous. This leads to that the jump of potential $\Delta\phi_w$ is constant on S_W. The integration on S_W can be performed explicitly and the jump $\Delta\phi_w$ can be linked to that at the trailing edge. Kutta condition is then used to determine the unknown $\Delta\phi_w$. This has been the foundation of the previous works of BEM for a hydrofoil. Morino and Kuo [2] for example divided the body surface into many flat elements with variables being assumed to be constant within each element. The jump $\Delta\phi_w$ at the trailing edge is assumed to be equal to the jump of the potentials at the centroids of the elements in contact with the trailing edge from the lower and upper surface respectively. This assumption in fact implies that the tangential velocity at the trailing edge is zero. This may be true for the total potential of a foil with non-zero inner angle at the trailing edge. For the disturbed potential, its tangential derivative is non-zero and is equal to that of the incoming flow. This neglected effect was included in the correction introduced by Lee [3], through adding a term $\mathbf{U}_\infty \cdot \mathbf{t}_{1N}$ to account for the change of velocity potential when transferring from the control points to the trailing edge, in which $\mathbf{U}_\infty$ is the velocity vector of incoming flow and $\mathbf{t}_{1N}$ is the position vector linking two control points.

The constant panel method has some inherent weakness. Kinnas and Hsin [4] showed that when N panels were used on the foil the error near the trailing edge will decay at the rate of $O(1/N)$. They proposed a correction due to the variation of the potential within the panel in the integral for the potential. As the variation was unknown before the potential was found, an iterative procedure was then used to solve the problem and the accuracy was improved. Apart the error form the assumption that variable is constant within each panel, using flat panel of model body surface

geometry itself will also introduce error. A detailed analysis of global error in the integral equation was given by Ezquerro et al. [5, 6]. Other typical work with low order BEM includes those by Maskew [7], Hess and Valarezo [8] and Kerwin et al. [9].

Compared with the low-order methods, the higher order boundary method (HOBEM) represents the variables within an element with a higher order function, together with the shape of the element itself. Hess [10] wrote local source distribution and panel shape in a Taylor series of a local coordinate. The derivatives in the Taylor expansion were obtained though the values of neighbouring nodes. Vaz et al. [11] used an integral equation of mixed source and dipole distribution, and their local strength together with the element shape were expanded into the Taylor series. They also undertook detailed error analysis. Instead of Taylor expansion, Kostas et al. [12] represented the source strength using the B-spline function. B-Spline together with the desingularization of the integral was also used by Lee et al. [13] for the foil. A review on the methods based on potential flow as well as boundary layer effect was given recently by Abidi et al. [14]

In the above works, the integral equation is established for the potential, in either lower or higher order boundary element methods. The kutta condition on the other hand is a condition on the velocity, or the derivative of the potential. This is often imposed numerically through the difference of the potentials at nodes near the trailing edge. Here in addition to the integral equation for the potential itself, we shall derive the integral equation of the tangential velocity. The two integral equations are used simultaneously, and the Kutta condition is imposed explicitly through the velocity. The body surface is first divided into curved panels, and slope is continuous at the node of each panel. The potential is expanded using the same higher order shape function within each element and the values of the potential and the velocity at the element nodes are the unknown coefficients which can be obtained by solving the integral equations for the potential and velocity simultaneously. This HOBEM does not lead to more computational effort than that based on the potential only. On the other hand, one of this advantages is that because the velocity is introduced in the solution procedure, it can deal with velocity based on the boundary conditions more easily and more accurately.

The paper is organized as follows. In Section 2, boundary integral equations for the potential and for the velocity are described. In Section 3, Numerical procedure including discretization of the boundary, expansion of the potential and appropriate choice of the shape function at the trailing edge is given. In Section 4, the numerical results are provided and discussed. In Section 5, the main conclusions are given.

2. Mathematical equations

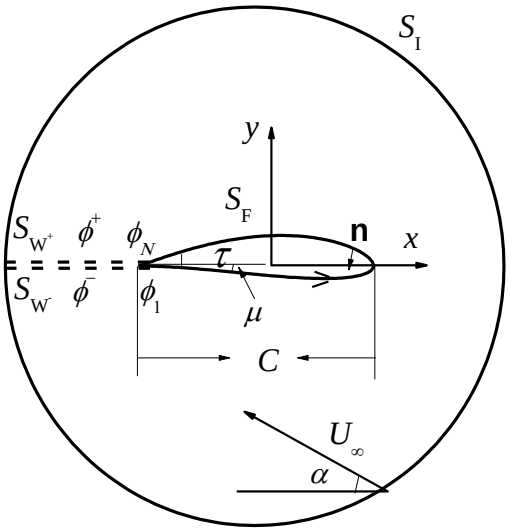

Fig. 1. Sketch of the problem

The problem of a body with sharp corner in a uniform current is considered and the hydrofoil is used as an example. We define a Cartesian coordinate system $O-xy$ with the origin at the midpoint of the chord of the foil, which is the line from leading edge to trailing edge. The uniform current with speed U is from the right hand side and it forms an angle α with the negative direction of x, as shown in Fig. 1. The foil has an inner angle τ at the trailing edge. μ is the angle at the trailing edge between its lower surface and the chord, or the x direction, and μ is positive when the lower surface is below the chord. It is assumed that the fluid is inviscid and the velocity potential theory can be adopted to describe the flow. When the fluid is incompressible the potential ϕ whose gradient is equal to the fluid velocity satisfies the Laplace equation

$$\nabla^2\phi = 0 \tag{1}$$

The body surface boundary condition and the far field boundary condition can respectively be written as

$$\phi_n = 0, \quad \text{on} \quad S_F \tag{2}$$

$$\phi \to -U_\infty(x\cos\alpha - y\sin\alpha), \quad R = \sqrt{x^2+y^2} \to \infty, \text{ on } \quad S_I \tag{3}$$

When the purely irrotational flow without any circulation is assumed, the velocity at the sharp trailing edge of the foil is infinite, which is unphysical. To reflect the physical reality, Kutta condition is applied at the trailing edge, which, through introducing circulation into the flow, is to enforce the finite velocity at the trailing edge (x_0, y_0), or

$$|\nabla\phi| < \infty, \quad at \quad (x_0, y_0) \tag{4}$$

As a result the velocity potential along the wake of the foil, extended from the trailing edge and shown through S_W in Fig.1, is discontinuous. This means that the potentials will be equal to ϕ^+ and ϕ^- when S_W is approached form the upper and lower sides, or S_{W^+} and S_{W^-}, respectively,

and $\phi^+ \neq \phi^-$. However the normal velocity across the wake must be continuous, required by the mass conservation, so must be the pressure.

Through Green's identity, the Laplace equation can be converted into an integral equation over the whole boundary $S = S_F + S_{W^+} + S_{W^-} + S_I$

$$-A(p)\phi(p)+\int_S [\phi(q)\frac{\partial G(p,q)}{\partial n} - \frac{\partial \phi(q)}{\partial n} G(p,q)]dS=0 \tag{5}$$

where $\mathbf{n}$ is the normal of the boundary pointing out of fluid domain. $G = \ln r_{pq}$ in Eq. (5) is the Green function for the two dimensional Laplace equation, where r_{pq} is the distance from the field point p to the source point q, $A(p)$ is the solid angle at the field point p. Using Eq. (3) for ϕ at infinity in the integration over the S_{I} in Eq. (5), the term will simply become $-2\pi U_\infty (x_p \cos\alpha - y_p \sin\alpha)$, where (x_p, y_p) are the coordinates of point p. On the wake, due to continuity of the normal velocity, we have $\phi_{n^+} = -\phi_{n^-}$. Furthermore from the continuity of the pressure, the tangential velocity across the wake for the steady flow is also continuous. This leads to that $\phi^+ - \phi^- = \phi_N - \phi_1$ where ϕ_N and ϕ_1 are the potentials at the trailing edge, approaching from the upper and lower surfaces respectively. This gives

$$\int_{S_{W^+}+S_{W^-}} \phi(q)\frac{\partial G(p,q)}{\partial n} dS = (\phi_1 - \phi_N)\int_{S_{W^-}} \frac{\partial G(p,q)}{\partial n^-} dS \tag{6}$$

Eq. (5) then becomes

$$-A(p)\phi(p) + \int_{S_F} [\phi(q)\frac{\partial G(p,q)}{\partial n} - \frac{\partial \phi(q)}{\partial n} G(p,q)]dS + (\phi_1 - \phi_N)W = 2\pi U_\infty (x_p \cos\alpha - y_p \sin\alpha) \tag{7}$$

where

$$W = \int_{-\infty}^{x_0} \frac{y_0 - y_p}{(x_q - x_p)^2 + (y_0 - y_p)^2} dx_q = -\mathrm{sgn}(y_p - y_0)\left[\tan^{-1}\frac{|y_p - y_0|}{x_p - x_0} + \pi H(x_0 - x_p)\right] \tag{8}$$

and $\mathrm{sgn(x)}$ and $H(x)$ are sign and step functions respectively. The step function is used in Eq. (8) because $\tan^{-1}$ is defined with $[-\pi/2, \pi/2]$. As $x_p > x_0$ when p is on the body surface, we have

$$W = -\tan^{-1}\frac{y_p - y_0}{x_p - x_0}, \quad x_p > x_0 \tag{9}$$

Eq. (7) can be used as a governing integral equation when p is on the body surface. At any smooth point $A(p) = \pi$. However, care is needed when p is at the trailing edge, as ϕ_1 at p_1 and ϕ_N at p_N are different, although the coordinates of p_1 and p_N are the same. In fact, the equation at trailing edge may be established in different ways, but the results will all be same. As shown in the appendix, we have at the trailing edge

$$-(\pi-\mu)\phi_1-(\pi-\tau+\mu)\phi_N+\int_{S_F}[\phi(q)\frac{\partial G(p,q)}{\partial n}-\frac{\partial\phi(q)}{\partial n}G(p,q)]dS \\ =2\pi U_\infty(x_p\cos\alpha-y_p\sin\alpha) \tag{10}$$

In the conventional boundary element method, Eq. (7) is the only one which is used. For example, when the constant element is used, the equation is imposed at the centre of each element. ϕ_1 and ϕ_N at the trailing edge are obtained from the values at centres of the adjacent elements, through which a condition on the tangential velocity is in fact implicitly implied.

In fact, Eq. (7) is an equation for the potential only, while the Kutta condition is imposed on the velocity. Here we shall introduce the velocity directly into the equation, which will allow the Kutta condition to be satisfied more accurately. As shown in Fig. 1, the tangential direction is positive following anti-clockwise direction and the normal is positive when pointing out of the fluid domain. This gives

$$\partial G/\partial n=-\partial H/\partial l \tag{11}$$

where

$$H(x_q-x_p,y_q-y_p)=\tan^{-1}\left[(y_q-y_p)/(x_q-x_p)\right]$$

and $n_x=-y_l$, $n_y=x_l$. Following the direction of l, we have $dl=dS$. Substituting Eq. (8) into Eq. (7), we have

$$\int_{S_F}\phi(q)\frac{\partial G(p,q)}{\partial n}dl=-\int_{p_1}^{p_N}\phi(q)\frac{\partial H(p,q)}{\partial l}dl=\int_{S_F}\phi_l(q)H(p,q)dl-(\phi_N-\phi_1)H(x_0-x_p,y_0-y_p) \tag{12}$$

The W term in Eq. (7) will then be cancelled by the last term in the above equation. Eq. (7) becomes

$$-A(p)\phi(p)+\int_{S_F}[\phi_l(q)H(p,q)-\frac{\partial\phi(q)}{\partial n}G(p,q)]dl=2\pi U_\infty(x_p\cos\alpha-y_p\sin\alpha) \tag{13}$$

Taking the tangential derivative of Eq. (13) with respect to p and using $\partial G/\partial n_p=-\partial H/\partial l_p$, then we have

$$A(p)\phi_{l_p}(p)+\int_{S_F}[\frac{\partial\phi(q)}{\partial l}\frac{\partial G(p,q)}{\partial n_p}+\frac{\partial\phi(q)}{\partial n}\frac{\partial G(p,q)}{\partial l_p}]dl=-2\pi U_\infty(x_{l_p}\cos\alpha-y_{l_p}\sin\alpha) \tag{14}$$

This gives an equation directly for the velocity. Different from Eq. (7) for the potential, it does not contain an integral from the wake. Also there is no need for special derivation when p is at the trailing edge, as done for the potential in appendix A. This is because ϕ_l is continuous at the trailing edge, or $\phi_l(p_1)=\phi_l(p_N)$ and the solid angle can be simply taken as $2\pi-\tau$. It may seem that the above derivation has made computation more complex as there are now two integral equations, or Eq. (7) and Eq. (14) for potential and velocity respectively, rather than a single equation, or Eq. (7) for the potential in the conventional method. However, with the help of Eq. (14), Kutta condition can be more accurately enforced. Also as we shall show below when these two

equations are used with the higher order element proposed in this work, it does not increase any additional computational effort compared with the normal higher order element method.

3. Computational procedure

In the numerical solution, the boundary S_F is divided into a series of small elements. On each element, the potential is expanded through shape function with unknown coefficients. In the normal higher order element methods, these coefficients are usually related to the nodal values of the potential. Here taking account into Eq. (14) for the velocity, we expand the potential within an element with nodes 1 and 2 containing nodal values of both potential and tangential velocity.

$$\phi(s)=\sum_{i=1}^{2}[\, f_i(s)\phi_i + l_0 g_i(s)\phi_{li}\,] \tag{15}$$

where

$$f_1=1-3s^2+2s^3,\quad f_2=3s^2-2s^3,\quad g_1=s-2s^2+s^3,\quad g_2=-s^2+s^3 \tag{16}$$

Here $s=l/l_0$, where l is the arc length coordinate from the first node of the element and l_0 is the length of the element. It can be easily confirmed that $\phi(s=0)=\phi_1$ and $\phi(s=1)=\phi_2$. Differentiating Eq. (15) along l, it can also be confirmed that $\phi_l(s=0)=\phi_{l1}$ and $\phi_l(s=1)=\phi_{l2}$. Therefore with the shape functions in Eq. (16), the continuities of the potential and the tangential velocities at the element nodes can be conveniently met. This allows the Kutta condition to be explicitly imposed together with Eq. (14).

When the mathematical form of the foil is available, it can be directly used in the integral equation. In general case, consistent with the potential, we may use the same function in Eq. (16) for the element shape as well. This ensures that the discretized boundary is continuous at element nodes, as well as the slope. Specifically, the body surface may be discretized into $N-1$ elements. The discretization of Eq. (10) takes the form of

$$\sum_{j=1}^{N}(H_{1j}^{q}\phi_j + L_{1j}^{q}\phi_{lj}) - A(p_1)\phi_1 - A(p_N)\phi_N = \int_{S_F}\frac{\partial\phi(q)}{\partial n}G(p,q)dl + 2\pi U_\infty(x_1\cos\alpha - y_1\sin\alpha) \tag{17}$$

where $A(p_1)=\pi-\mu$ and $A(p_N)=\pi-\tau+\mu$. At field points $i=2,\cdots N-1$, we have from Eq. (7)

$$\sum_{j=1}^{N}(H_{ij}^{q}\phi_j + L_{ij}^{q}\phi_{lj}) + (\phi_1-\phi_N)W - A(p)\phi_i = \int_{S_F}\frac{\partial\phi(q)}{\partial n}G(p,q)dl + 2\pi U_\infty(x_i\cos\alpha - y_i\sin\alpha) \tag{18}$$

and from Eq. (14)

$$\sum_{j=1}^{N}(H_{ij}^{p}\phi_j + L_{ij}^{p}\phi_{lj}) - A(p)\phi_{li} = \int_{S_F}\frac{\partial\phi(q)}{\partial n}\frac{\partial G(p,q)}{\partial l_p}dl + 2\pi U_\infty(x_{li}\cos\alpha - y_{li}\sin\alpha) \tag{19}$$

where

$$H_{ij}^{q} = l_{0j}\int_0^1 f_1\frac{\partial G(p,q)}{\partial n_q}ds + l_{0\,j-1}\int_0^1 f_2\frac{\partial G(p,q)}{\partial n_q}ds$$

$$L_{ij}^{q} = l_{0j}^2\int_0^1 g_1\frac{\partial G(p,q)}{\partial n_q}ds + l_{0\,j-1}^2\int_0^1 g_2\frac{\partial G(p,q)}{\partial n_q}ds$$

$$H_{ij}^{p} = -\int_0^1 f_{s1} \frac{\partial G(p,q)}{\partial n_p} ds - \int_0^1 f_{s2} \frac{\partial G(p,q)}{\partial n_p} ds$$

$$L_{ij}^{p} = -l_{0j} \int_0^1 g_{s1} \frac{\partial G(p,q)}{\partial n_p} ds - l_{0j-1} \int_0^1 g_{s2} \frac{\partial G(p,q)}{\partial n_p} ds$$

in which $q \in (j, j+1)$ for the first term, while $q \in (j-1, j)$ for the second term. The term of ϕ_n on the right hand sides of Eqs. (17-19) are known based on a given boundary condition. In the present case, it is zero because of Eq. (2). Eqs. (17-19) are enforced at all nodes, or $i = 1, \cdots N-1$, which gives $2N-2$ equations. Here locations of nodes 1 and N are the same and they are both located at the trailing edge. Due to circulation, ϕ_N and ϕ_1 are different. The velocity at the trailing edge is continuous due to the Kutta condition. Therefore there are $2N-1$ unknowns, or one more than the number of equations. We note that for a non-zero inner angle τ, from continuities of the pressure and velocity at the trailing edge, it can be easily established that the trailing edge must be a stagnation point, or $\phi_l = 0$. In such a case, there will be $2N-2$ unknowns, the same as the number of equations.

Generally, the use of above discretization together with the shape function in Eq. (16) can give highly accurate results, provided the number of elements used is sufficient. However for the foil problem the accurate prediction of the flow near the trailing edge is crucially important as it affects greatly the overall results. To achieve that, the shape function used must be compatible with the local flow characters. Based on the Laplace equation and the impermeable body surface boundary condition, we can write the potential near the trailing edge generally as

$$\phi = A_0 + \sum_{n=1}^{\infty} A_n r^{t_n} \cos\left[t_n(\theta - \tau + \mu)\right] \tag{20}$$

where (r, θ) is the polar coordinate system with the origin at the trailing edge, $\theta = 0$ is along the chord, and

$$t_n = n\pi / (2\pi - \tau) \tag{21}$$

The first term gives infinite velocity when $r = 0$. When the Kutta condition is imposed, we shall have $A_1 = 0$ and the remaining leading terms will be t_2 and t_3 terms, which give the finite velocity at the trailing edge. Thus to reflect the behaviour of the potential, within element 1, the shape functions in Eq. (16) can be modified as

$$f_1 = 1 + \frac{(t_2 s^{t_3} - t_3 s^{t_2})}{t_1}, \quad f_2 = \frac{-t_2 s^{t_3} + t_3 s^{t_2}}{t_1}, \quad g_2 = l_0 \frac{s^{t_3} - s^{t_2}}{t_1} \tag{22}$$

together with $\phi_{l1} = 0$. Similar expansion can be used to element $N-1$. The crucial difference between Eq. (22) and Eq. (16) is that $\phi_l \to l^{\tau/(2\pi-\tau)}$ in the former and $\phi_l \to l$ when $l \to 0$ at the trailing edge. Although both of them tend to zero, the former reflects the true behaviour of the potential. More importantly, the ϕ_{ll}, or the derivative of the velocity at the trailing edge is infinite

based Eqs. (20) and (22), while it is finite based on Eq. (16). Therefore such a seemly small difference in the exponent makes a big difference to the accuracy of local results, and subsequently overall results.

When p is a smooth point, singularities of G and its derivative when $q \to p$ in the Green function can be easily treated by many well established methods. Attention is once again needed when p is at the trailing edge. Assume that p approaches the tip from element *N*-1, or point p_N at node N. The tangential direction l_p and n_p in Eq. (5) then correspond to p_N. Within element $N-1$, when q approaches p_N, $\partial G(q, p_N)/\partial n_N$ will be finite and is related to the curvature at p_N. Therefore it is in fact not a singularity. However, when q approaches p_1 at node 1, this becomes very different because of the sharp angle. As the normal and tangential directions at p_1 and p_N are different, $\partial G(q, p_1)/\partial n_N$ is different from $\partial G(q, p_1)/\partial n_1$. When $q \to p_1$, the latter is non-singular, which is similar to $\partial G(q, p_N)/\partial n_N$. However, for the former, it is singular. To deal with that, we can write locally

$$x_q - x_1 = x_{l1} l + 0.5 x_{ll1} l^2 \tag{23}$$

$$y_q - y_1 = y_{l1} l + 0.5 y_{ll1} l^2 \tag{24}$$

where subscripts *l* and *ll* indicate the first and the second derivatives respectively. Substituting them into $\partial G(q, p_1)/\partial n_N$, it yields

$$\frac{\partial G(q, p_1)}{\partial n_N} = \frac{C_1}{l_0 s} + C_2 \tag{25}$$

where $C_1 = y_{lN} x_{l1} - x_{lN} y_{l1}$ and $C_2 = y_{lN} x_{ll1} - x_{lN} y_{ll1}$. Because of the sharp corner at the trailing edge, $C_1 \neq 0$ or the normal direction (x_{lN}, y_{lN}) at p_N is not perpendicular to the tangential direction (x_{l1}, y_{l1}) at p_1. Using the shape functions in (22), the integration of $\frac{\partial G(q, p_1)}{\partial n_N}$ over element 1 can be written as

$$\int_{S_1} \frac{\partial G(q, p_1)}{\partial n_N} \phi_l dl = [(C_1 t_2 t_3 / l_0 + C_2)(\phi_2 - \phi_1) - C_1 \phi_{l2}] / [(t_2 - 1)(t_3 - 1)] \tag{26}$$

This then has effectively removed the singularity. Once all the singular behaviours are treated, the remaining integrations in Eqs. (17-19) can be calculated through Gaussian method. When field point p is near the trailing edge, the source point q can be very close to p at nearby elements. For example, node 2 could be very close to element $N-1$. To ensure accuracy, the integration step has to be much smaller than the distance between q and p. In this work, if not specified, we have used 64 points for the integration to achieve that.

4. Numerical Results

We use the Karman-Trefftz (KT) foil to show the effectiveness and the accuracy of the present

method. We will first show that the results are quite inaccurate if the local shape function at the trailing edge is not chosen properly. It is important that the choice should match the behaviour of the local flow and with the shape function suggested in the present work the results are highly accurate. We then show that when the conventional BEM is used directly, the predicted velocity near the trailing edge is far less accurate than that obtained from the present method.

The KT section is produced from the conformal mapping of a circle in the complex ζ -plane into complex plan $z = x + y\mathbf{i}$, as shown in Fig. 2. The circle centered at $\zeta_c=(\xi_c,\eta_c)$ has a radius r_c and passes through the point (-1, 0). The transformation takes the form of [15, 16]

$$z=\frac{\lambda[(\zeta+1)^{\lambda}+(\zeta-1)^{\lambda}]}{(\zeta+1)^{\lambda}-(\zeta-1)^{\lambda}} \tag{27}$$

where $\lambda=2-\frac{\tau}{\pi}$ and τ is the inner angle of the foil at the trailing edge. Here point (-1, 0) in the ζ plane corresponds to the trailing edge $(-\lambda,0)$ in the z plane, and $(2\xi_c+1,0)$ to $(x_g,0)$ where x_g can be obtained from (27). The distance between two intersection points of the foil with the x axis is $C = x_g + \lambda$ and it can be adjusted through ξ_c and λ. The angle $\mu = \pi - \tan^{-1}\frac{\eta_c}{\xi_c+1} - \frac{\pi\lambda}{2}$, which is negative when the lower surface of the hydrofoil is above the x axis. Here the coordinate system $O-xy$ may not be exactly the same as that described in Fig.1. However, the equations derived above will be the same in these two systems apart from a constant in the equation for the potential, which can be incorporated into the potential and does not affect the velocity. The analytical solutions for the potential and the velocity can be found in the work by Kinnas and Hsin [4].

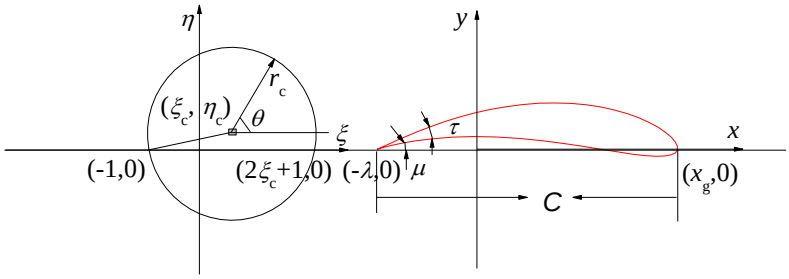

Fig. 2. The KT transformation

4.1 The effect of local shape function at the trailing edge

Shape functions (16) can be used at most of elements, apart from the elements connecting the trailing edge. Even when the velocity is no longer singular, the derivative of the velocity and subsequently the derivative of the pressure can still be singular. This means that the velocity changes very rapidly. To capture the local behaviour of the velocity at the trailing edge, shape function in (22) is used here. We now use (16) and (22) respectively as the shape functions for the trailing edge and run the simulations for the same problem. We take $\xi_c = 0.1$, $\eta_c = 0$ and $\tau=10^{\circ}$, which

corresponds to $\lambda = 1.94$ and $\mu = 5^\circ$. The attack angle of the incoming flow is taken as α=5°. r_c and U are used for nondimensionalisaton, and therefore they are both taken as unit. The circle in the ζ plane is uniformly divided into $N_e = N - 1$ elements and the coordinates of each node are transformed to the physical plane through Eq. (27). The element length attached to the trailing edge in z plane follows $\Delta\theta^\lambda$, where $\Delta\theta = 2\pi / N_e$. Here $1 \le \lambda < 2$, and this means when N_e increases, the size of the element attached to the trailing edge decreases much faster. Results are given in Fig. 3, in which l is measured along the foil surface from the lower trailing edge to the upper trailing edge in the anti-clockwise direction. It can be seen when (21) is used, 40 elements are sufficient to provide results which are graphically indistinguishable with the analytical solution, both for the potential and the velocity. On the other hand, when (16) is used at the trailing edge, major difference between the numerical results and the analytical solution can be observed. It is most interesting to see that very large error occurs near the leading edge. When the number of elements is doubled to $N_e = 80$, the difference decreases but it is still quite large. When N_e is quadruple to 160, the difference is still very significant, which indicates that the convergence is very slow if it ever does. This shows that it is very important to choose the shape function at the trailing edge properly. It should reflect the true behaviour of the variation of the velocity near the trailing edge. The figure also shows that the choice introduced in this work is highly effective and efficient.

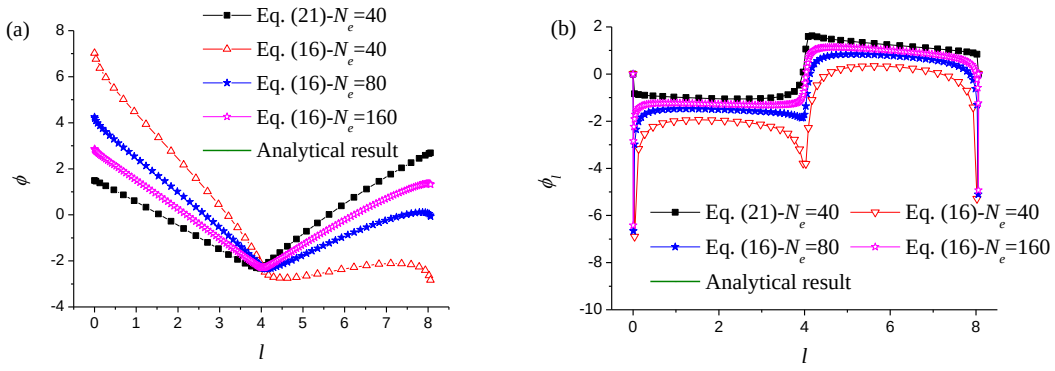

Fig. 3. The effect of the local shape function: (a) velocity potential ϕ and (b) tangential velocity ϕ_l (τ=10°, $\mu = 5^\circ$, α=5°).

4.2 Comparisons between the present HOBEM, conventional BEM and analytical results

In the conventional BEM, the integral equation is used only for the potential. When constant shape function is used for each element, the equation is imposed at the centre of each element. The simplest way to impose the Kutta condition when $\tau \neq 0$ is to let ϕ_1 and ϕ_N at the trailing edge be equal to the values of the potentials at the centres of elements 1 and $N-1$ respectively. In BEM here we use the linear shape function, and let $\phi_1 = \phi_2$ and $\phi_N = \phi_{N-1}$. The boundary integral equation is then imposed from node 2 to node N-2. When the potential ϕ is found, the tangential velocity ϕ_l can be obtained through three point finite difference method. In the following cases,

comparisons between the present HOBEM, conventional BEM and analytical results are made at different: (1) attack angle of flow α, (2) angle μ and (3) inner angle τ.

(1) At different attack angle α

The foil which we consider corresponds to $\xi_c = 0.1$, $\eta_c = 0.1$, $\tau = 10^\circ$ and $\mu = -0.19^\circ$. From Eqs. (17) and (18), we can see the potential at an attack angle α can be obtained from $\phi = \phi_0 \cos\alpha - \phi_{90} \sin\alpha$, where ϕ_0 and ϕ_{90} are the solutions at $\alpha = 0$ and $\alpha = \pi/2$ respectively. This means that the computations are needed only for these two angles. For a real problem, the inviscid steady potential is valid only at a relatively small angle. Therefore we shall use ϕ_0 and ϕ_{90} to investigate accuracy for α being set as 0°, 5°, 10° and 15° respectively. The body is divided into $N_e = 40$ elements in HOBEM, and into 40, 80 and 160 elements respectively in BEM.

Figs. 4 and 5 provide the difference between numerical results and analytical solution at α=0° and 90°, respectively. For $\alpha = 0$, when 40 elements are used in HOBEM, the error in potential along the foil surface is more uniform. In comparison, there is a jump of error in the potential near the trailing edge. The jump becomes milder when the number of elements increases, as can be seen in Fig. 4(a). For $\alpha = 90^\circ$ in Fig. 5(a), the result from HOBEM at $N_e = 40$ is quite accurate, while the error in the result from BEM is very noticeable. The error in BEM will decrease when N_e increases, However, at $N_e = 160$, the results are still less accurate that those from HOBEM at $N_e = 40$. The difference between HOBEM and BEM becomes much more obvious for the velocity, as can be seen in Figs. 4(b) and 5(b). While the HOBEM gives very accurate results at $N_e = 40$, Fig. 4(c) shows that the error in the tangential velocity at the point next to the trailing edge is very significant and does not even decrease noticeably when N_e increases, and remains significant even at $N_e = 160$. In Fig. 5(c), the largest error of BEM occurs near the leading edge ($l \approx 4$), although it decreases when N_e increases.

As shown in Table 1, when $\alpha = 0^\circ$, the average errors of HOBEM and BEM in ϕ are comparable at $N_e = 40$. When $\alpha = 90^\circ$, however, the error of HOMEM is two magnitude lower than that of BEM. Even when N_e is increased to 160, the error of BEM is still higher than that of HOBEM at $N_e = 40$. For the velocity, at both $\alpha = 0^\circ$ and $\alpha = 90^\circ$, only when $N_e = 160$ the error of BEM becomes comparable with that of HOBEM at $N_e = 40$. For the largest error in Table 2, the pattern of error for ϕ is similar to that in Table 1. For the velocity, the error of BEM is very significant. It hardly decays with N_e when $\alpha = 0^\circ$ for the reason noticed in Fig.4(c). It may decay at $\alpha = 90^\circ$ but the decay is very slow. On the other hand, the error of HOBEM is small at $N_e = 40$.

The error at other attack angles can be obtained from the combination of those corresponding to ϕ_0 and ϕ_{90}. The results are shown in Tables 3 and 4. It is interesting to see from the above results that the present HOBEM method has significantly improved the accuracy of velocity prediction. For the potential the BEM may provide results of accuracy comparable with HOBEM in some cases along most part of the body, especially when $\alpha \approx 0^\circ$. However overall it is less accurate than HOBEM in most cases. In particular it becomes far less accurate near the trailing edge or leading edge.

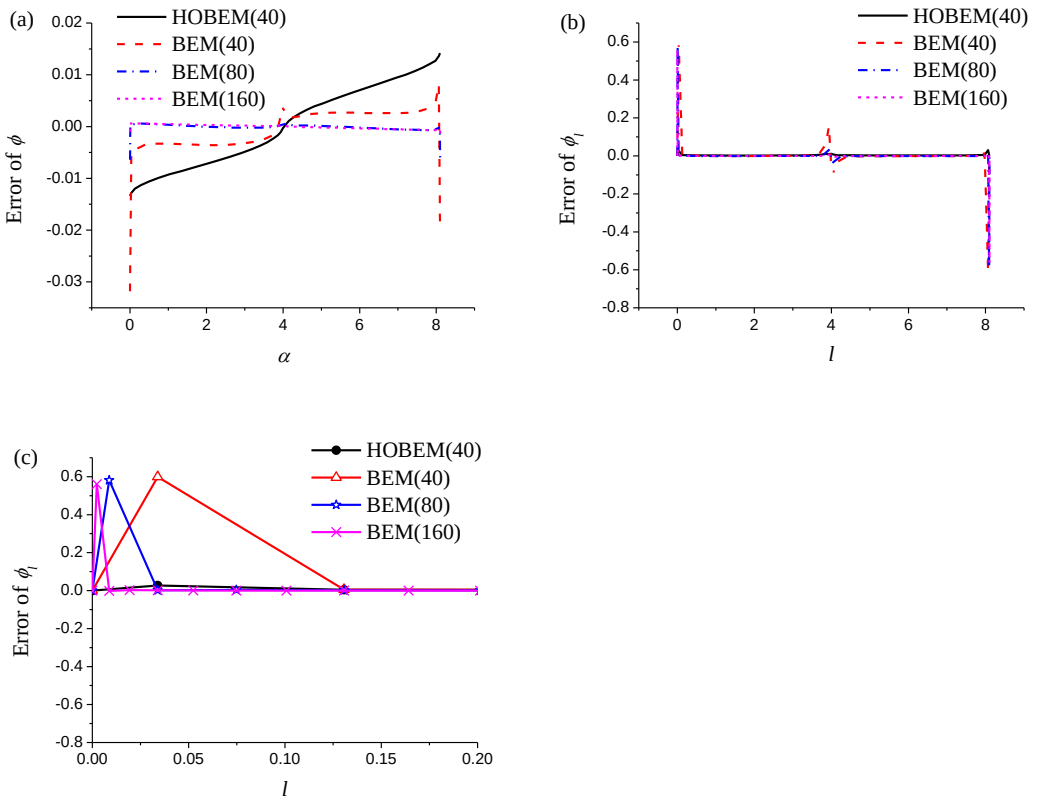

Fig. 4. Errors at $\alpha = 0^\circ$: (a) ϕ, (b) ϕ_l, (c) blow up of ϕ_l near trailing edge between $l = 0$ and 0.2

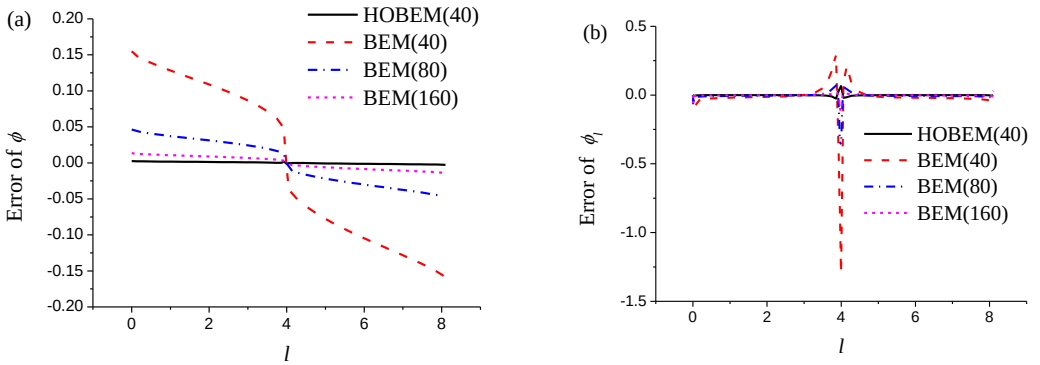

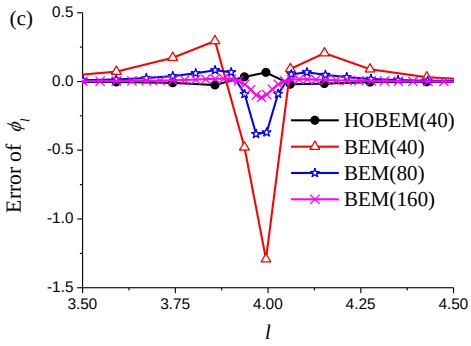

Fig. 5. Errors for $\alpha = 90^\circ$: (a) ϕ, (b) ϕ_l, (c) blow up of ϕ_l near leading edge between $l = 3.5$ and 4.5

Average	$\phi(0)$	$\phi(90)$	$\phi_l(0)$	$\phi_l(90)$
HOBEM(40)	7.07×10^{-3}	1.31×10^{-3}	4.9×10^{-3}	5.1×10^{-3}
BEM(40)	4.14×10^{-3}	1.03×10^{-1}	4.19×10^{-2}	8.22×10^{-2}
BEM(80)	4.75×10^{-4}	2.94×10^{-2}	1.8×10^{-2}	2.43×10^{-2}
BEM(160)	3.58×10^{-4}	8.34×10^{-3}	8×10^{-3}	6.76×10^{-3}

Table 1. Average error at $\alpha = 0^\circ$ and 90°

Largest	$\phi(0)$	$\phi(90)$	$\phi_l(0)$	$\phi_l(90)$
HOBEM(40)	1.42×10^{-2}	2.7×10^{-3}	3.04×10^{-2}	6.55×10^{-2}
BEM(40)	3.18×10^{-2}	1.58×10^{-1}	6.11×10^{-1}	1.29
BEM(80)	6.5×10^{-3}	4.75×10^{-2}	5.86×10^{-1}	3.82×10^{-1}
BEM(160)	2.2×10^{-3}	1.4×10^{-2}	5.63×10^{-1}	1.15×10^{-1}

Table 2. Largest error at $\alpha = 0^\circ$ and 90°

Average α	ϕ(HOBEM)	ϕ(BEM)	ϕ_l(HOBEM)	ϕ_l(BEM)
5°	6.94×10^{-3}	6.91×10^{-3}	4.85×10^{-3}	4.4×10^{-2}
10°	6.75×10^{-3}	1.51×10^{-2}	4.77×10^{-3}	4.65×10^{-2}
15°	6.51×10^{-3}	2.37×10^{-2}	4.67×10^{-3}	4.97×10^{-2}

Table 3. Average error at the attack angle α between 0° and 90°

Largest α	ϕ(HOBEM)	ϕ(BEM)	ϕ_l(HOBEM)	ϕ_l(BEM)
5°	1.39×10^{-2}	3.26×10^{-2}	2.99×10^{-2}	6.08×10^{-1}
10°	1.35×10^{-2}	2.24×10^{-2}	2.92×10^{-2}	6.01×10^{-1}
15°	1.3×10^{-2}	5.89×10^{-2}	2.83×10^{-2}	5.88×10^{-1}

Table 4. Largest error at the attack angle α between 0° and 90°

(2) At different μ

We next consider hydrofoils of different angle μ. We set $\xi_c = 0.1$, $\alpha = 10^\circ$, $\tau = 10^\circ$. μ is chosen as 5°, -0.19° and -5.3° by taking η_c as 0, 0.1 and 0.2 respectively. The foil shapes are depicted in Fig. 6, $\mu = 5^\circ$ corresponds to a symmetric foil, $\mu = -0.19^\circ$ to a foil with a nearly horizontal lower surface near the trailing edge, and for $\mu = -5.3^\circ$, the lower surface of foil is above the horizontal axis.

Fig. 6. The foil shape ($\xi_c = 0.1$, $\tau = 10^\circ$): (a) $\eta_c = 0 (\mu = 5^\circ)$, (b) $\eta_c = 0.1 (\mu = -0.15^\circ)$, (c) $\eta_c = 0.2 (\mu = -5.3^\circ)$

Figs. 7-9 provide the difference between numerical results and analytical solution at $\mu = 5^\circ$, $\mu = -0.19^\circ$ and $\mu = -5.3^\circ$ respectively. For $\mu = 5^\circ$ in Fig. 7(a), the foil is symmetric, and the result of potential from HOBEM at $N_e = 40$ is quite accurate. While the error in the result from BEM is very significant, it will decrease as N_e increases, and at $N_e = 160$ it becomes comparable with that from HOBEM at $N_e = 40$. For the asymmetric foils at $\mu = -0.19^\circ$ and -5.3°, in Figs. 8(a) and 9(a), the error of HOBEM is larger than that in the symmetric case, but its variation along the body is smooth. The error in BEM jumps near the trailing edge. This shows that this kind of jump of error occurs at different μ, as at different α.

Tangential velocities are provided in Figs. 7(b), 8(b) and 9(b). At all these μ, large error in BEM generally occurs at the trailing edge ($l = 0$ and $l \approx 8$) and also at the leading edge ($l \approx 4$). In particular, in the local close up, shown in Figs. 7(c), 8(c), 9(c), although the error decreases when N_e increases, the reduction of error is rather small and the error is still significant at $N_e = 160$. In fact the error at $N_e = 160$ is still larger than that at $N_e = 40$ of HOBEM.

Tables 5 and 6 give average and largest errors respectively. When $N_e = 40$, the average error of HOBEM is much lower than that of BEM at $\mu = 5^\circ$ and -0.19°, and they are comparable at $\mu = -5^\circ$. In terms of the largest error, the HOBEM is much more accurate than the BEM in all cases. Once again, the largest error of BEM in the velocity does not change very much when N_e increases, as can be seen in Figs. 7(c), 8(c) and 9(c).

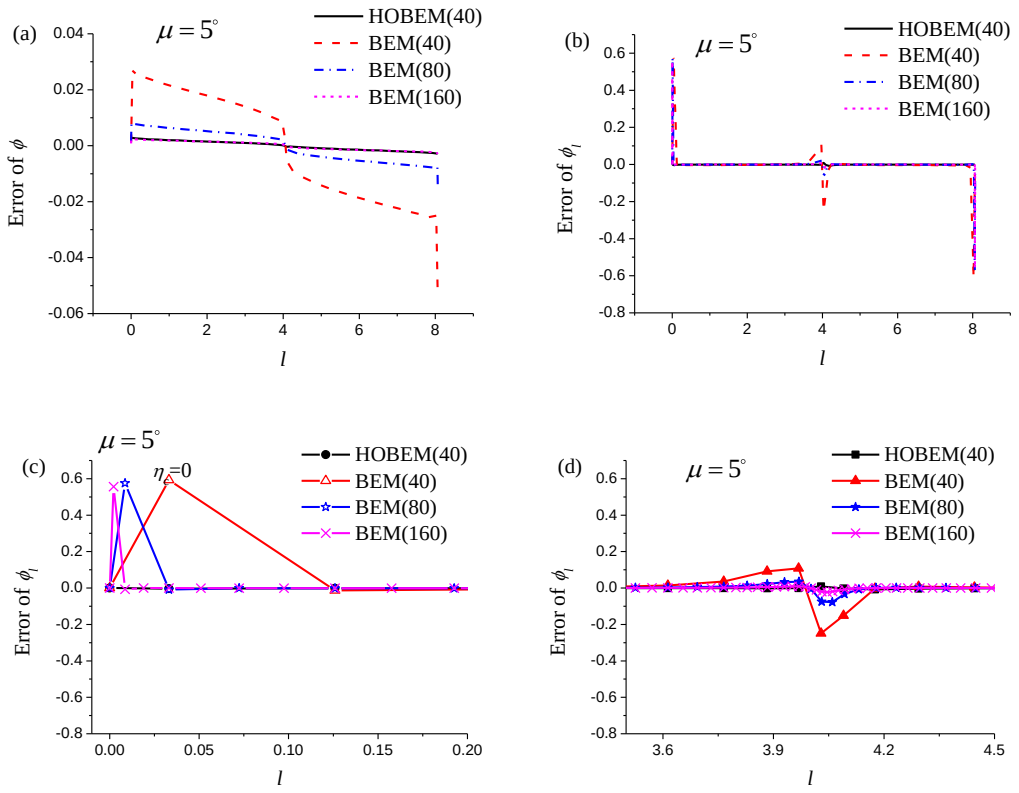

Fig. 7. Errors at $\mu = 5^\circ$: (a) ϕ, (b) ϕ_l, (c) blow up of ϕ_l near trailing edge, and (d) blow up of ϕ_l near the leading edge

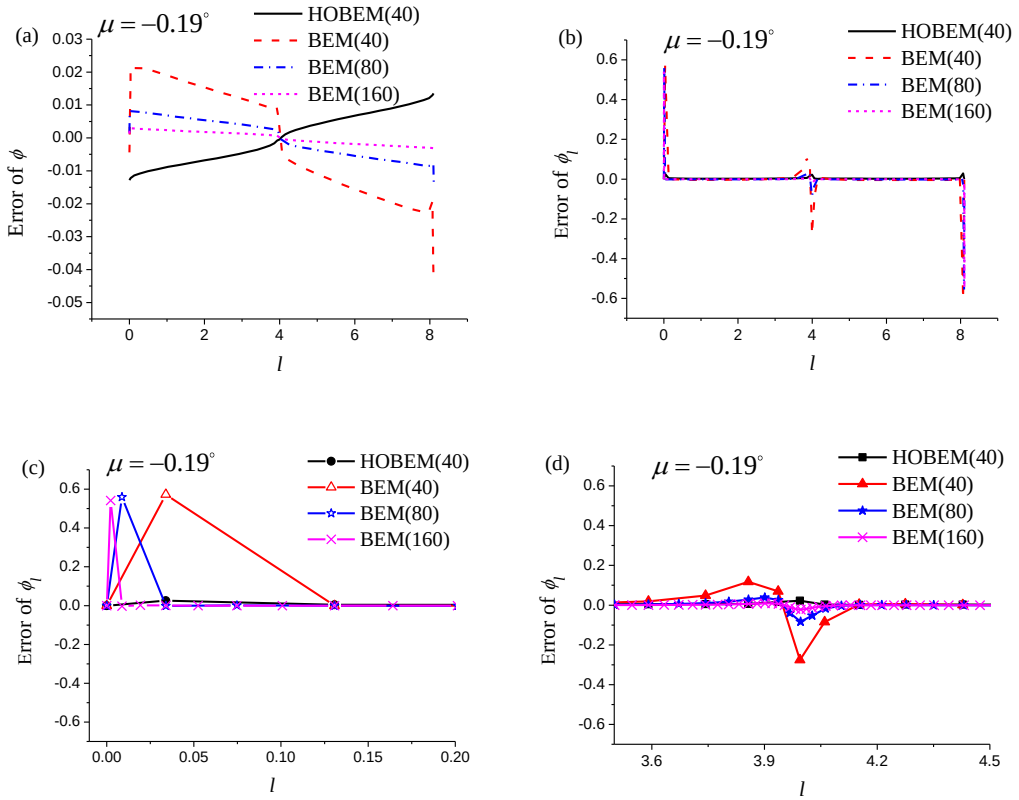

Fig. 8. Errors at $\mu = -0.19^{\circ}$: (a) ϕ, (b) ϕ_l, (c) blow up of ϕ_l near trailing edge, and (d) blow up of ϕ_l near the leading edge

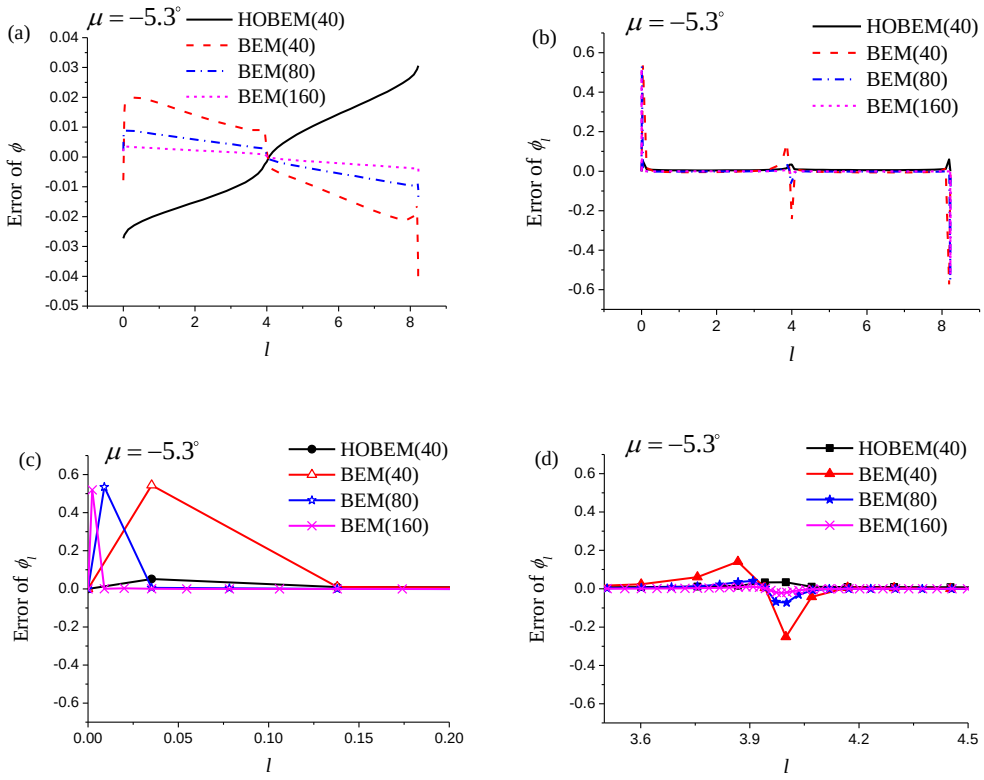

Fig. 9. Errors at $\mu = -5.3^{\circ}$: (a) ϕ, (b) ϕ_l, (c) blow up of ϕ_l near trailing edge, and (d) blow up of ϕ_l near the leading edge

Error	$\eta_c = 0 (\mu = 5^{\circ})$		$\eta_c = 0.1 (\mu = -0.19^{\circ})$		$\eta_c = 0.2 (\mu = -5.3^{\circ})$	
	ϕ	ϕ_l	ϕ	ϕ_l	ϕ	ϕ_l
HOBEM(40)	1.48×10^{-3}	1.26×10^{-3}	6.75×10^{-3}	4.77×10^{-3}	1.49×10^{-2}	1.02×10^{-2}
BEM(40)	1.76×10^{-2}	4.78×10^{-2}	1.51×10^{-2}	4.65×10^{-2}	1.36×10^{-2}	4.41×10^{-2}
BEM(80)	5.07×10^{-3}	1.92×10^{-2}	5.25×10^{-3}	1.92×10^{-2}	5.59×10^{-3}	1.89×10^{-2}
BEM(160)	1.44×10^{-3}	8.3×10^{-3}	1.78×10^{-3}	8.28×10^{-3}	2.13×10^{-3}	8.21×10^{-3}

Table 5. Average errors at different μ ($\xi_c = 0.1, \tau = 10^{\circ}$, $\alpha = 10^{\circ}$)

Error	$\eta_c = 0 (\mu = 5^{\circ})$		$\eta_c = 0.1 (\mu = -0.19^{\circ})$		$\eta_c = 0.2 (\mu = -5.3^{\circ})$	
	ϕ	ϕ_l	ϕ	ϕ_l	ϕ	ϕ_l
HOBEM(40)	2.9×10^{-3}	8.8×10^{-3}	1.35×10^{-2}	2.92×10^{-2}	3.06×10^{-2}	6.01×10^{-2}
BEM(40)	5.18×10^{-2}	6.09×10^{-1}	4.6×10^{-2}	6.01×10^{-1}	4.18×10^{-2}	5.82×10^{-1}
BEM(80)	1.44×10^{-2}	5.83×10^{-1}	1.45×10^{-2}	5.72×10^{-1}	1.5×10^{-2}	5.52×10^{-1}
BEM(160)	2.4×10^{-3}	5.6×10^{-1}	4.6×10^{-3}	5.48×10^{-1}	5.3×10^{-3}	5.27×10^{-1}

Table 6. Largest errors at different μ ($\xi_c = 0.1, \tau = 10^\circ$, $\alpha = 10^\circ$)

(3) At different τ

We next consider hydrofoils of different inner angle τ at 5°, 10° and 20° respectively at a fixed angle $\mu = 0^\circ$. Based on the relationship $\tau = 2\left(\tan^{-1}\frac{\eta_c}{\xi_c + 1} + \mu\right)$ in KT foil, different τ at $\mu = 0^\circ$ can be obtained by setting η_c as 4.8027×10^{-2}, 9.6238×10^{-2} and 1.9396×10^{-1} respectively at $\xi_c = 0.1$. The attack angle of the incoming flow α is set as 10°. The shapes of these three hydrofoils are provided in Fig. 10. As τ increases, the upper surface of the foil rises gradually, and the foil becomes more asymmetric.

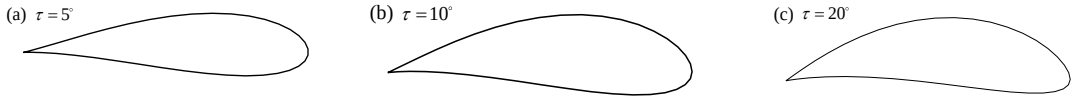

Fig. 10. The shape of the foil ($\xi_c = 0.1$): (a) $\tau = 5^\circ$ ($\eta = 4.8027\times10^{-2}$), (b) $\tau = 10^\circ$ ($\eta = 9.6238\times10^{-2}$), (c) $\tau = 20^\circ$ ($\eta = 1.9396\times10^{-1}$)

Figs.11-13 provide the error in $\tau = 5^\circ$, 10° and 20° respectively. The trend is very similar to the previous cases at different α and different μ. Overall the HOBEM with $N_e = 40$ gives accurate results for velocities of all the foils, While BEM can give accurate results over most part of the foil when N_e increases, the error near the trailing edge and leading edge decays very slowly. In particular for the point next to the trailing edge, the error does not seem to decay very much when the N_e has been increased by four times. The comparison of accuracies of BEM and HOBEM can be more clearly seen in tables 7 and 8. For the average error in velocity, only when $N_e = 160$ the accuracy of BEM becomes comparable to that of HOBEM at $N_e = 40$. For the largest error in velocity, the error of HOBEM at $N_e = 40$ is one order lower than that of BEM at $N_e = 160$.

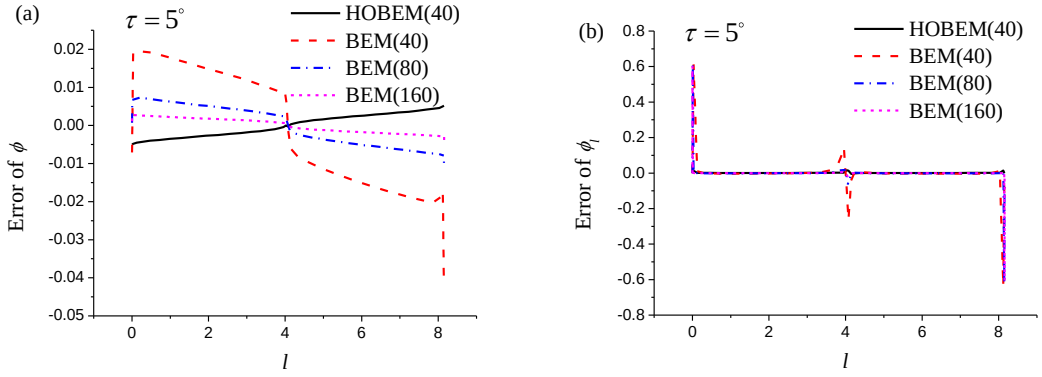

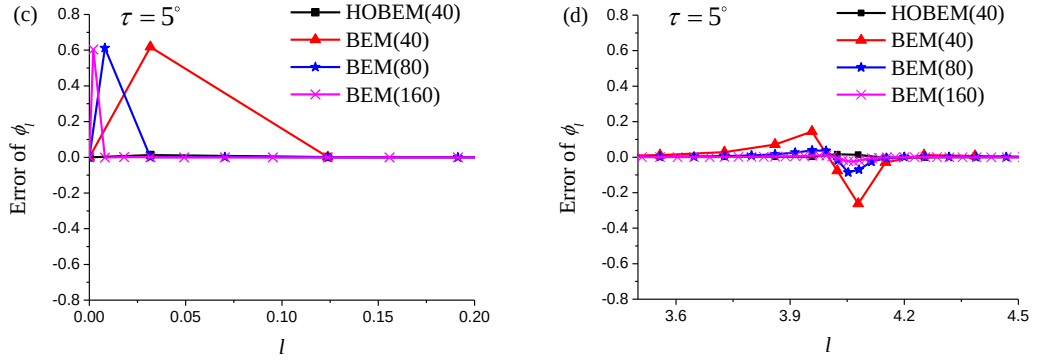

Fig. 11. Errors at $\tau = 5^\circ$: (a) ϕ, (b) ϕ_l, (c) blow up of ϕ_l near trailing edge, (d) blow up of ϕ_l near the leading edge

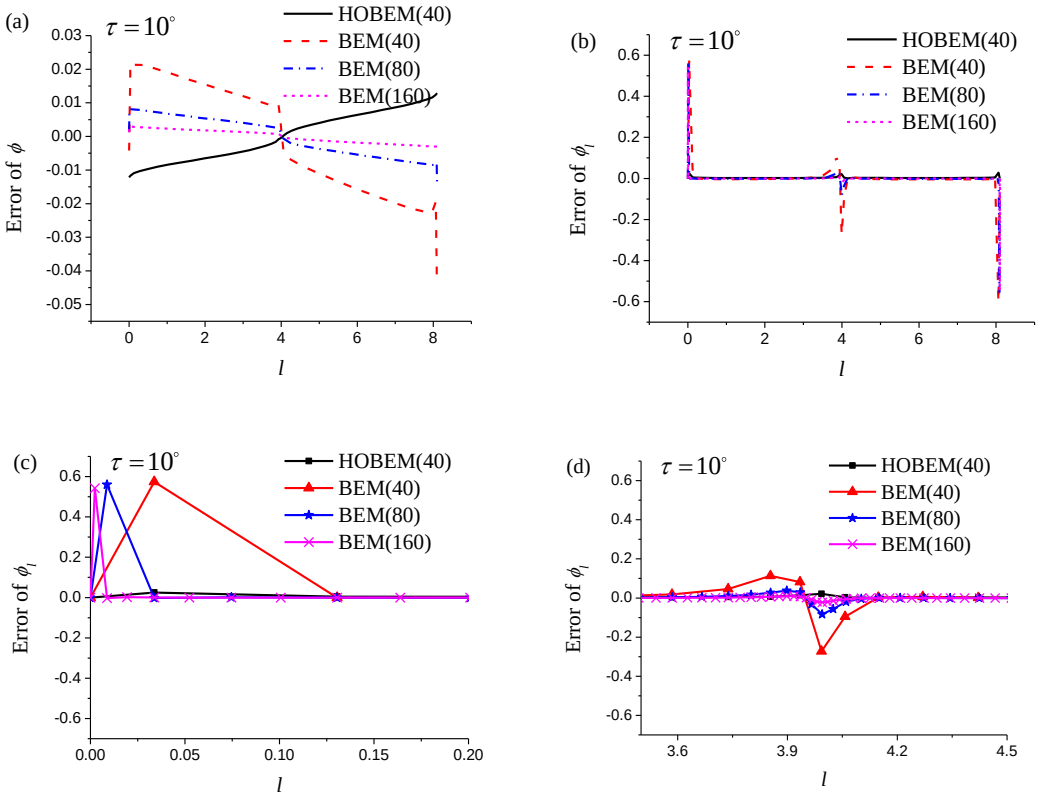

Fig. 12. Errors at $\tau = 10^\circ$: (a) ϕ, (b) ϕ_l, (c) blow up of ϕ_l near trailing edge, (d) blow up of ϕ_l near the leading edge

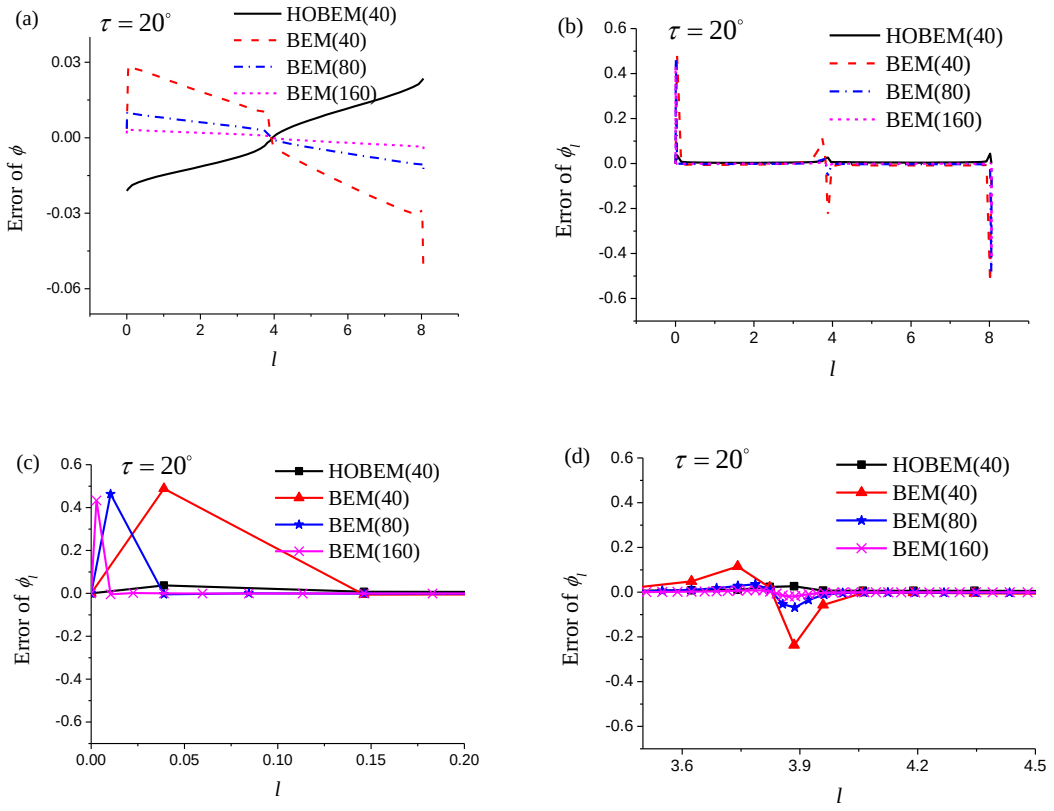

Fig. 13. Errors at $\tau = 20^\circ$: (a) ϕ, (b) ϕ_l, (c) blow up of ϕ_l near trailing edge, (d) blow up of ϕ_l near the leading edge.

Error	$\tau = 5^\circ$		$\tau = 10^\circ$		$\tau = 20^\circ$	
	ϕ	ϕ_l	ϕ	ϕ_l	ϕ	ϕ_l
HOBEM(40)	2.63×10^{-3}	2.43×10^{-3}	6.44×10^{-3}	4.55×10^{-3}	1.15×10^{-2}	7.75×10^{-3}
BEM(40)	1.45×10^{-2}	4.81×10^{-2}	1.52×10^{-2}	4.68×10^{-2}	1.83×10^{-2}	4.15×10^{-2}
BEM(80)	4.87×10^{-3}	2.04×10^{-2}	5.24×10^{-3}	1.92×10^{-2}	6.07×10^{-3}	1.7×10^{-2}
BEM(160)	1.7×10^{-3}	8.99×10^{-3}	1.76×10^{-3}	8.29×10^{-3}	1.94×10^{-3}	7.03×10^{-3}

Table 7. Average errors at different τ ($\xi_c = 0.1$, $\mu = 0^\circ$, $\alpha=10^\circ$)

Error	$\tau = 5^\circ$		$\tau = 10^\circ$		$\tau = 20^\circ$	
	ϕ	ϕ_l	ϕ	ϕ_l	ϕ	ϕ_l
HOBEM(40)	5.2×10^{-3}	1.45×10^{-2}	1.29×10^{-2}	2.8×10^{-2}	2.35×10^{-2}	4.42×10^{-2}
BEM(40)	4.4×10^{-2}	6.37×10^{-1}	4.61×10^{-2}	6.01×10^{-1}	5.4×10^{-2}	5.3×10^{-1}
BEM(80)	1.36×10^{-2}	6.21×10^{-1}	1.45×10^{-2}	5.73×10^{-1}	1.67×10^{-2}	4.82×10^{-1}
BEM(160)	4.4×10^{-3}	6.08×10^{-1}	4.6×10^{-3}	5.48×10^{-1}	5.1×10^{-3}	4.42×10^{-1}

Table 8. Largest errors at different τ ($\xi_c = 0.1$, $\mu = 0^\circ$, $\alpha=10^\circ$)

5. Conclusions

A higher order boundary element method is presented, based on the conventional boundary integral equation for the velocity potential and a similar equation for tangential velocity derived in this paper. Within each element the velocity potential is expressed in terms of higher order shape functions, together with the nodal values of the potential and tangential velocity. The continuities of the potential and velocity are ensured at element nodes, and the Kutta condition is imposed at the trailing edge through the velocity directly, together with a special shape function to account for the behaviour of the local velocity. Extensive simulations have been undertaken for Karman-Trefftz (KT) foil, from which the following conclusions can be drawn.

(1) For HOBEM involving velocity, the shape function used near the trailing edge should account for the local behaviour of the velocity.

(2) Error in BEM jumps rapidly near the trailing edge and this may also occur near the leading edge for the velocity. There is no jump of error in HOBEM.

(3) For the velocity, the accuracy of HOBEM is much higher than that of BEM, even when much more elements are used in BEM. Near the trailing edge in particularly, HOBEM can give accurate result for the velocity with a relatively small number of elements, while the error in BEM remains significant, even though four times more elements are used. The decay of error in BEM is very slow near the trailing edge.

(4) The present method can be used to solve many other problems more accurately, where the continuity of the velocity at element nodes are important, or the boundary condition explicitly contains tangential velocity.

Acknowledgements

This work is supported by Lloyd's Register Foundation to which the authors are most grateful. Lloyd's Register Foundation helps to protect life and property by supporting engineering-related education, public engagement, and the application of research.

This work is also supported by the National Natural Science Foundation of China (Grant No. 51879123, 51809123).

Appendix

We first consider the following integration

$$\begin{aligned} &-\int_a^b \frac{\eta_p}{(\xi_q-\xi_p)^2+\eta_p^2}\,d\xi_q \\ &= -\mathrm{sgn}(\eta_p)\left(\tan^{-1}\left\{\frac{|\eta_p|(b-a)}{[\eta_p^2+(b-\xi_p)(a-\xi_p)]}\right\}+\pi H[-\eta_p^2-(b-\xi_p)(a-\xi_p)]\right) \\ &= -(\pi-\theta) \end{aligned} \tag{A.1}$$

with the figure below

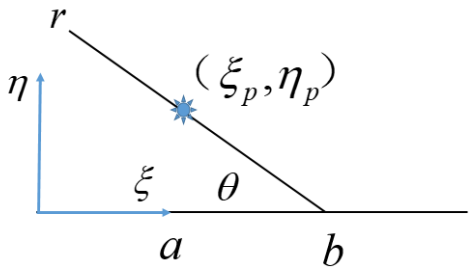

Fig. A.1. The integration for a field point p approaching to an element at an angle θ where $\xi_p = b - r\cos\theta$, $\eta_p = r\sin\theta$ and ξ and η are along and normal to the element.

Point p can approach the trailing edge in three different ways.

(1) Let p be on the lower surface and p approach p_1. We have $A(p) = \pi$ where $p \to p_1$ but $p \neq p_1$. Also when $p \to p_1$, from Eq. (8), we have $W = \mu$. In the integration of Eq. (7), when q is along the lower surface and near p_1, the Cauchy principal integration is taken as the point $q = p$ has already considered by $\pi\phi(p)$. However, when q is along the upper surface and near p_N, the integration should be equal to Cauchy principal integration plus the point $q = p$. Using Eq. (A.1) in which ξ is from node N-1 to N, and $\theta = \tau$, the latter gives $-(\pi - \tau)\phi_N$. Thus Eq. (7) for $p = p(x_0, y_0)$ can be written as

$$\int_{S_F} [\phi(q)\frac{\partial G(p,q)}{\partial n} - \frac{\partial \phi(q)}{\partial n} G(p,q)]dS - (\pi - \mu)\phi_1 - (\pi - \tau + \mu)\phi_N = 2\pi U_\infty (x_p \cos\alpha - y_p \sin\alpha) \tag{A.2}$$

Here the Cauchy principle integration will be taken when q approaches the trailing edge from both lower and upper surfaces.

(2) Let p be on the upper surface and near p_N. Similar to the analysis above, we have $A(\mathrm{p}) = \pi$, $W = -(\tau - \mu)$, and there will be a contribution $-(\pi - \tau)\phi_1$ from the integration along the lower surface near p_1. As a result, it also gives Eq. (A.2).

(3) Let p be at the trailing edge. Then when we derive Eq. (5), the following path near the trailing edge shown in Fig. A.2 below

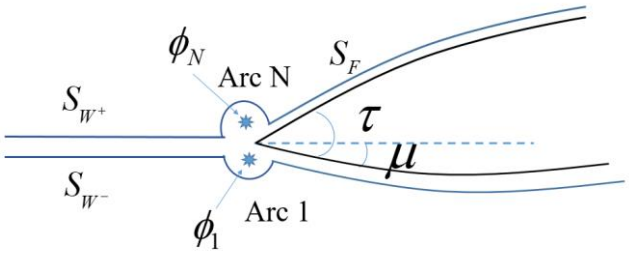

Fig. A.2. Integral path for p at the trailing edge.

should be taken. Then for the arc centred at p_1 we have

$$\phi_1 \int_{Arc1} \frac{\partial G(p,q)}{\partial n_q} dS = (\pi - \mu)\phi_1 . \tag{A.3}$$

Similar for p_N, the result will be $(\pi - \tau + \mu)\phi_N$. Also $W = 0$ in this case as $y_p - y_0 = 0$ is taken in the integrand. Therefore the result will be also (A.2).

References

[1] Newman JN. Marine Hydrodynamics, 40th Anniversary Edition. MIT press; 1977.

[2] Morino L, Kuo CC. Subsonic Potential Aerodynamics for Complex Configurations: A General Theory. AIAA J 1974; 12(2): 191-7.

[3] Lee JT. A potential based panel method for the analysis of marine propellers in steady flow. Massachusetts Institute of Technology;1987.

[4] Kinnas SA, Hsin CY. The Local error of a low-order boundary element method at the trailing edge of a hydrofoil and its effect on the global solution. Comput Fluids 1994; 23(1): 63-75.

[5] Ezquerro JM, Laverón-Simavilla A, Lapuerta V, Porter J. Global error analysis of two-dimensional panel methods for dirichlet formulation. Eng Anal Bound Elem 2017; 74: 88-99.

[6] Ezquerro JM, Lapuerta V, Laverón-Simavilla A, Fernández JJ. Global error analysis of two-dimensional panel methods for Neumann formulation. Eng Anal Bound Elem 2018; 95: 40-52.

[7] Maskew B. Prediction of subsonic aerodynamic characteristics: A case for low-order panel methods. J Aircraft 1982; 19(2): 157–163.

[8] Hess JL, Valarezo WO. Calculation of steady flow and propellers by means of a surface panel method. In 23rd Aerospace Sciences Mtg, AIAA, Reno, NV; 1985.

[9] Kerwin JE, Kinnas SA, Lee JT, Shih WZ. A surface panel method for the hydrodynamic analysis of ducted propellers. The Society of Naval Architects and Marine Engineers; 1987.

[10] Hess JL. Higher order numerical solution of the integral equation for the two-dimensional Neumann problem. Comput Methods Appl Mech Eng 1973; 2: 1-15.

[11] Vaz G, Falcão de Campos JAC, Eça L. A numerical study on low and higher-order potential based BEM for 2D inviscid flows. Comput Mech 2003; 32: 327–35.

[12] Kostas KV, Ginnis AI, Politis GG, Kaklis PD. Shape-optimization of 2D hydrofoils using an Isogeometric BEM solver. Computer-Aided Design 2017; 82: 79–87.

[13] Lee CS, Kerwin JE. A B-spline higher order panel method applied to two-dimensional lifting problem. J Ship Res 2003; 47 (4): 290–298.

[14] Abidi E, Hcini C, Kamoun B. A Survey on the Potential Flow/Boundary Layer Coupling Methods Applied to Airfoils. Arch Comput Methods Eng 2020; 27: 1-14.

[15] Milne-Thomson LM. Theoretical aerodynamics (4th edition). Dover Publication; 1973.

[16] Blom JJH. Some Characteristic Quantities of Karman-Trefftz Profiles. NASA Technical Memorandum TM-77013; 1983.